Dynamic multiple-target tracing to probe spatiotemporal cartography of cell membranes

Arnauld Sergé[1–3], Nicolas Bertaux[4–6], Hervé Rigneault[4,5] & Didier Marguet[1–3]

Although the highly dynamic and mosaic organization of the plasma membrane is well-recognized, depicting a resolved, global view of this organization remains challenging. We present an analytical single-particle tracking (SPT) method and tool, multiple-target tracing (MTT), that takes advantage of the high spatial resolution provided by single-fluorophore sensitivity. MTT can be used to generate dynamic maps at high densities of tracked particles, thereby providing global representation of molecular dynamics in cell membranes. Deflation by subtracting detected peaks allows detection of lower-intensity peaks. We exhaustively detected particles using MTT, with performance reaching theoretical limits, and then reconnected trajectories integrating the statistical information from past trajectories. We demonstrate the potential of this method by applying it to the epidermal growth factor receptor (EGFR) labeled with quantum dots (Qdots), in the plasma membrane of live cells. We anticipate the use of MTT to explore molecular dynamics and interactions at the cell membrane.

Knowledge of the dynamic organization of plasma membrane components is crucial for a better understanding of cellular functions. One fundamental question remains as to how the spatiotemporal organization of the membrane regulates signaling upon physiological stimulation. The development of experimental approaches used to study these structure-function relationships has remained challenging[1–4], with presently available techniques requiring a compromise between temporal and spatial resolution.

Among classical approaches, fluorescence recovery after photobleaching is based on ensemble-averaging measurements within a small area of the cell membrane[2]. Fluorescence correlation spectroscopy (FCS) provides a good alternative as it can be used to quantify translational diffusion with high temporal resolution and statistical accuracy[4]. Recently, we increased the strength of FCS by obtaining spatial information from measurements performed at variable observation volumes[5]. This approach can be used to detect the dynamic partitioning into nanodomains or the presence of a meshwork in live cells[6]. FCS observation, however, is still limited to a small area of the plasma membrane.

Single-molecule techniques such as SPT provide high spatial resolution, with molecular motion not masked by ensemble averaging[3,7]. When connecting moving tags, however, fast particles become difficult to connect at high densities: nearest neighbors are usually favored when ambiguities arise resulting, for instance, from particles appearing, disappearing or crossing paths. This drawback can be reduced both experimentally, using a high-quality, dedicated apparatus (optics, electron-multiplying charge-coupled device (CCD) camera, biomaterials and others), and analytically, by optimizing the algorithms. The introduction of fluorescent Qdots with high photostability, brightness and biolabeling versatility[8] has considerably increased the sensitivity of detection and greatly facilitated biological investigations of cellular processes[9,10]. The ability to trace a large number of targets would expand the potential of single-molecule approaches; the resulting larger number of observations would concurrently improve statistical relevance. Although it would be challenging, an approach that allows tracking particles at high densities and with fast acquisition speed is required to achieve an appropriate spatiotemporal resolution. Unfortunately, overcrowded datasets increase the occurrence of false detection or connection, and reducing illumination time directly degrades the signal-to-noise ratio (SNR).

Here we present a method for high-density labeling, MTT. Classically, SPT analyses are performed in two independent stages: peak detection and estimation, and trace reconnection[11,12]. In MTT, appropriate statistical tools provide optimal peak characterization. Introducing a deflation loop by subtracting detected peaks allows detection of additional peaks that were previously masked because of their lower intensity. Another improvement comes from the intrinsic link between detection and connection: analyses are alternately performed using information obtained at both stages. Therefore, accurate localization and exhaustive detection, combined with integrated historical information of trajectories, provide efficient multiple-target reconnection. Robustness is achieved by including minimum hypotheses on the underlying diffusion phenomena and by having to adjust a minimal set of parameters. Reconnection, in turn, allows validation of detected particles. To illustrate the tracking results, we detected for each trajectory

[1]Centre d'Immunologie de Marseille-Luminy, Université de la Méditerranée, [2]Institut National de la Santé et de la Recherche Médicale, Unité Mixte de Recherche 631, [3]Centre National de la Recherche Scientifique, UMR 6102, Parc scientifique de Luminy, Case 906, F-13288 Marseille cedex 09, France. [4]Institut Fresnel, Université Paul Cézanne, [5]Centre National de la Recherche Scientifique, UMR 6133, Domaine Universitaire de Saint Jérôme, F-13397 Marseille cedex 20, France. [6]École Centrale Marseille, Technopôle de Château-Gombert, 38, rue Frédéric Joliot Curie, F-13451 Marseille cedex 20, France. Correspondence should be addressed to D.M. (marguet@ciml.univ-mrs.fr).

RECEIVED 26 NOVEMBER 2007; ACCEPTED 6 JUNE 2008; PUBLISHED ONLINE 6 JULY 2008; DOI:10.1038/NMETH.1233

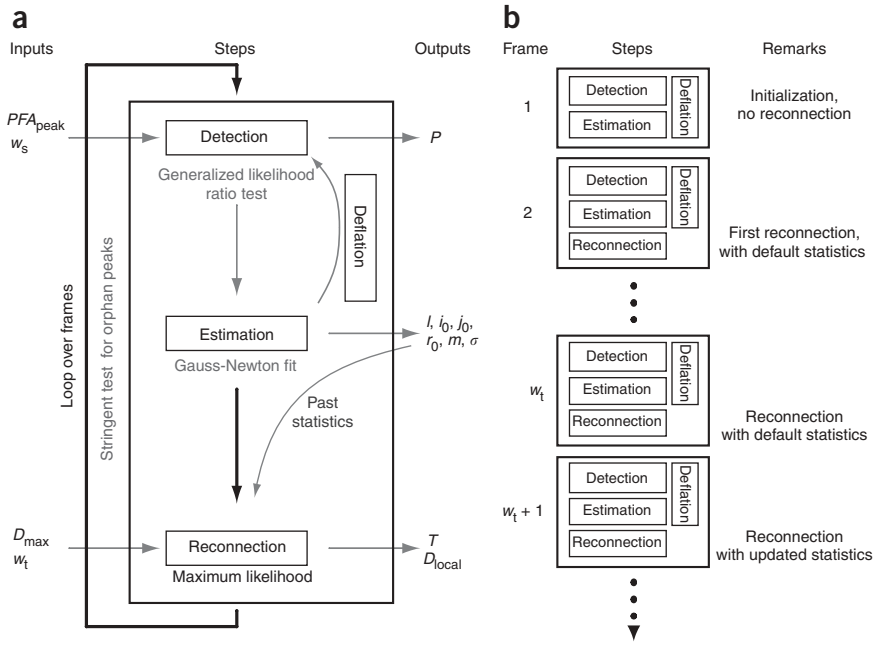

Figure 1 | Schematic overview of MTT. (**a**) Detailed description of the steps iteratively performed for each frame, with the main input and output parameters. Note that D_{max} is the major input parameter directly depending on the given biological system. For a broad range of initial conditions, all other inputs (that is, PFA_{peak}, which directly determines PD_{peak}, w_s, w_t and parameters of statistical laws) only have to be set once. After reconnection, orphan peaks are tested using a more stringent PFA_{orphan} before initiating new trajectories. (**b**) Frame-by-frame process of a full stack, illustrating the specificities concerning frames 1 and 2 (initiation of reconnection) and 1 to w_t (building of past statistics). From frame 1 to w_t, statistics (mean and variance of peak parameters) are assigned to default typical values, until they can be evaluated, over w_t past frames.

possible confinement within diffusive events, a key parameter of membrane dynamics. Combining analytical tools allowed us to track particles at higher densities and collect snapshots and movies of cell membrane organization over a short period of time (~10 s). This new conceptual approach introduces a general method of studying molecular dynamics for various constraints of speed or scale. We tested MTT by analyzing the membrane dynamics of EGFR[13] naturally expressed in COS-7 cells. Our work demonstrates the potential usefulness of MTT in analyzing membrane dynamics under physiological conditions.

RESULTS

Schematic principle of the MTT algorithm

SPT is based on the ability to accurately identify the center of a peak. By imaging isolated fluorescent molecules, spatial resolution close to the molecular scale can be achieved, and it is possible to construct trajectories of these fluorescent molecules (which we call reconnection) as long as they remain visible. But it is challenging to do this at high particle density and low SNR. In this work we overcame these challenges and simultaneously tracked a large number of molecules. In MTT, the detection, estimation of positions and reconnection are done sequentially (**Fig. 1**). First, MTT provides efficient detection of particles, and second, it takes into account past information for the reconnection. A mathematical description is available in the **Supplementary Note** online.

Individual fluorophores behave as point-source emitters and generate blurred images described by the point-spread function (PSF) of the microscope. Classically, the image of each fluorophore can be described by the fluorescence level $X_{i,j}$ at pixel (i,j), which results from the sum of a fluorescence peak, offset and noise[11,12]:

$$X_{i,j} = I \times G_{i,j}(i_0, j_0, r_0) + m + N_{i,j}(\sigma^2), \quad (1)$$

where I is the intensity of the particle, G is a bidimensional Gaussian modeling the PSF centered in (i_0,j_0) with a radius r_0 (**Supplementary Note**), m corresponds to the mean background intensity and N models the background noise of s.d., σ (**Supplementary Table 1** online).

For any given image, I is unknown and represents a random variable with a probability distribution including the phenomena of photon noise, bleaching and blinking. Bleaching is negligible for fluorescent markers such as Qdots because their lifespan is longer than the acquisition time[8]. Blinking is more critical as it is present

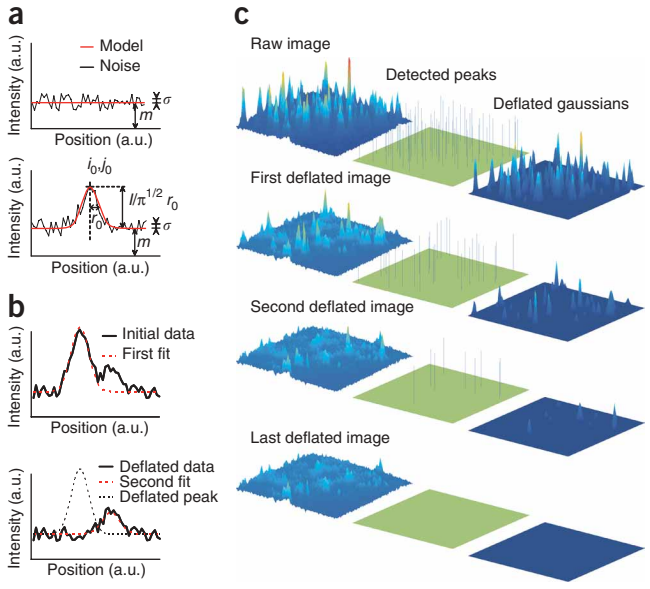

Figure 2 | Exhaustive particle detection principle. (**a**) A GLRT compares H_0/H_1 hypotheses. In H_0, the window contains only Gaussian noise with s.d. σ and mean offset m; in H_1, the window also contains a Gaussian peak centered in (i_0,j_0), with a radius r_0 and an intensity I (leading to an amplitude $I/\pi^{1/2}r_0$). (**b**) Window containing two peaks of different intensities ($I_1/I_2 = 3$). A first fit detects the most intense peak (top). Deflation allows the minor peak, initially buried, to be detected next (bottom). All graphs depict simulated fluorescence intensity against spatial position as a line-scan through an image. (**c**) Deflation scheme applied to an image from Qdots-EGFR on COS-7 cells. From the raw image (top left, 3D representation of the fluorescence signal), all identified peaks (top center, binary map of detections; top right, Gaussian fits) are subtracted, providing a first deflated image (second row, left image). This is repeated as long as peaks are detected.

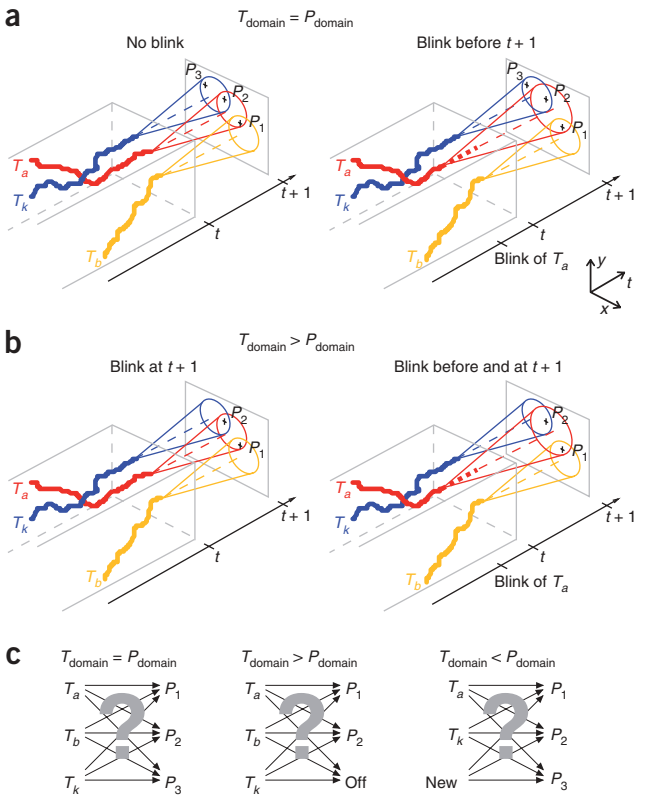

Figure 3 | Multiple-target reconnection. (**a**,**b**) MTT searches for the best combinations between T_{domain} known trajectories and P_{domain} peaks detected from the next image, according to descriptors (I, D and others) and projected statistics (δI, δD and others). In **a**, $T_{domain} = P_{domain}$ (left). The particles that belong to the maximum reconnection domain of T_k, are expected within a circle of radius $R = 3r_{max}$ for statistical confidence. This maximum distance between two frames, r_{max}, corresponds to a particle diffusing at D_{max} without any constraint. If T_k was previously turned off (right), the domain is increased according to $R^2 = (3r_{max})^2\, t_{off}$, with t_{off} being the number of elapsed frames since the particle turned off. In **b**, $T_{domain} > P_{domain}$ owing to particles blinking at $t + 1$ (or $T_{domain} < P_{domain}$, for particles appearing; data not shown), with the possibility of past blinking (right). (**c**) Combinatorics of the maximum-likelihood reconnection test.

at all time scales from nanoseconds to seconds[14]. There are three possible scenarios: (i) the particle may be constantly 'on' during one (or several) image(s); (ii) it may have blinked (one or several times) on time scales smaller than the acquisition time, leading to an intermediate fluorescence intensity; or (iii) the particle may have disappeared, having been turned off (fully blinked) during one (or several) image(s) (**Supplementary Fig. 1** online). For a completely 'on' particle, the experimental distribution and variability correspond to a Gaussian distribution centered on an average intensity $\langle I_{on} \rangle$. When particles are partially turned off, we add a second term (uniform law) describing the equal probability for all blinking values. The third case (particle turned off) has no relevant contribution to the likelihood of reconnection as no signal is detected.

According to equation 1, the background of an image is a mix of thermal noise, photon noise and autofluorescence from the sample. It is modeled as independent background m in addition to a Gaussian noise N of unknown power σ^2. The parameters m and σ^2 are assumed to be locally constant (**Supplementary Fig. 1**).

MTT iteratively reconstructs trajectories up to time t (**Fig. 1**). Past statistics are used to accurately reconnect trajectories at the next time point, $t + 1$. For each trajectory, in addition to the last position, MTT characterizes the parameters of the following probability laws, (i) the local diffusion coefficient D_{local} (**Supplementary Table 1**), (ii) the mean and s.d. of the intensity and (iii) the photophysical state relative to blinking (**Supplementary Fig. 1**).

Exhaustive particle detection and estimation by deflation

At high particle densities, exhaustive detection is critical as missing or false particles will directly compromise all the later steps in the analysis. Therefore, MTT has to minimize errors. Detection and estimation are completed by a deflation loop.

Particle detection is classically performed using a bi-dimensional Gaussian approximating the microscope PSF[15]. For each image, first, an optimal detection test is applied to screen for the presence of Gaussian peaks. The usual statistical test is a generalized likelihood ratio test (GLRT; **Supplementary Note**). The image intensity is analyzed in a sliding window in which the respective probabilities of particle presence (H_1) or absence (H_0) are compared, taking into account the image noise: targets are no longer identified by the fluorescence intensity but by the H_1/H_0 ratio (**Fig. 2a**). This ratio is high when peaks are significantly separated from noise as evaluated by the algorithm. A window size w_s of 7×7 pixels ensures a correct estimation of the background while limiting possible long-range background variations. The accuracy of the decision is set by fixing a constant false-alarm rate. To ensure a probability of false alarm (PFA_{peak}) of less than 1 for an image of 512×512 pixels, we set the GLRT with a constant PFA_{peak} of 10^{-6}. This strategy provides a high confidence level for all detected particles, insuring that they do not arise from the noise. Notably, the PFA_{peak} is independent of the intensity and background, and consequently of the experimental image acquisitions. Finally, w_s and PFA_{peak} are the only two parameters required for detection.

This step only provides a binary detection. Identified peaks then need to be properly estimated for each relevant parameter such as intensity, subpixel position, width and offset. They are evaluated by a multi-parametric Gaussian fit on the signal intensity. Filtering tests remove putative aberrant points (that is, negative intensity or positions out of the sliding window).

Particles with low intensity can potentially be misdetected owing to neighboring particles of stronger intensity within the window, mainly leading to background overestimation (**Fig. 2b**). We therefore carried out a deflation process. Starting from P_{frame} particles already detected in the current frame, we subtracted their respective estimated Gaussian peaks from the raw image X_{in} as follows:

$$X_{out} = X_{in} - \sum_{p=1}^{P_{frame}} I_p \times G(i_p, j_p, r_p). \qquad (2)$$

We reiterated the detection and estimation processes on the resulting image (**Fig. 2c**) until we detected only noise, illustrating the efficiency of detection.

Optimized reconnection using past information

We selected an approach that avoids both the limitation of a local strategy and the lengthy computation time of a fully global strategy. For each trajectory, MTT searches either for an association with a particle detected in the subsequent frame or for possible blinking. To limit the factorial growth of the reconnection combinatorics, we

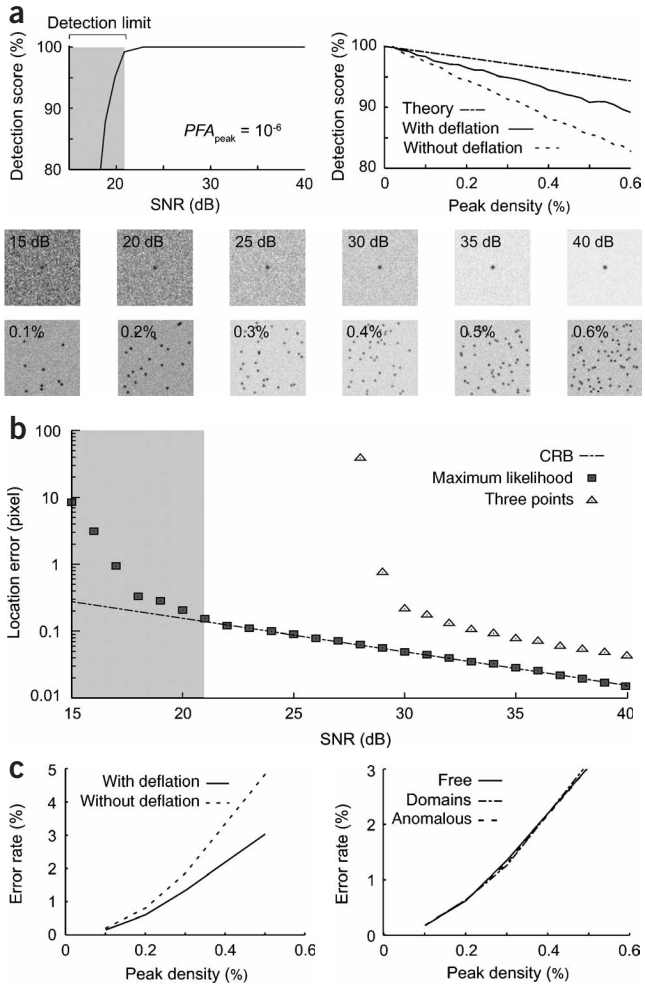

Figure 4 | Performances of the deflation algorithm for detection, estimation and reconnection. (**a**) Percentage of detected peaks (with correct estimation), relative to initial peak density, according to SNR (left) and peak density theoretical or measured, using deflation or not (SNR = 30 dB; right). Images correspond to Monte Carlo simulations with varying SNR or peak density (percent peak per pixel, in 100 × 100 pixel images, at $PFA_{peak} = 10^{-6}$). (**b**) Maximum-likelihood localization accuracy for increasing SNR, as compared to a three-point estimator and the theoretical limit given by Fisher coefficients and associated Cramer-Rao bound (CRB) to determine estimation efficiency. Location accuracy in the shaded area was no longer optimal with respect to the CRB. (**c**) Reconnection efficiency of MTT performed with or without deflation (left) or applied to free, confined by domains or anomalous diffusion (right) for increasing peak density (SNR = 30 dB). The error by trace is evaluated by comparing the input (simulated) and output (reconnected) trajectories. This was ultimately checked by direct visual inspection.

restricted the set to trajectories and particles with sufficient reconnection probabilities. Conflicts between trajectories are then optimally resolved using statistical information from each trajectory.

For each trajectory T_k, a reconnection domain was defined by the area potentially explored by a particle after one time lag. To delineate the domain, we assume a Brownian motion with a maximum diffusion coefficient D_{max}. This provides a limit for reconnection without making assumptions about the real diffusion mode of the particles. Thus, the domain is a disk, defined by a probability law, which is a bidimensional Gaussian with a s.d. r_{max}. A cutoff set at $3r_{max}$ ensures 99% confidence of finding particles (**Supplementary Fig. 2** and **Supplementary Video 1** online). In the most favorable case, the reconnection is unambiguous with only one peak within an isolated reconnection domain. However, when trajectories are crossing, conflicting overlap may occur between reconnection domains sharing at least one particle. Thus, MTT evaluates the probability of each possible combination attributing T_{domain} trajectories to P_{domain} particles, including possible blinking. In the simplest case where $T_{domain} = P_{domain}$ (**Fig. 3a**), T_k will not blink (or will turn on again) at time $t + 1$. If $T_{domain} > P_{domain}$ (**Fig. 3b**), one or more candidate trajectories blink at time $t + 1$. On the contrary, $T_{domain} < P_{domain}$ signifies that new trajectories appear. In all cases, we consider that blinking, acting on all time scales, will occur with the same probability for all particles.

MTT then validates the most probable reconnection among all possible combinations (**Fig. 3c**). Starting from a set of particles and trajectories, MTT searches for the best combination based on a comparison of probabilities between each (T_i,P_j) association. The probability of each association is the product of the statistics computed for their respective positions, intensities and blinking. Here the descriptors of trajectories are not built only from the last frame. Instead, the use of several frames allows an evaluation of their probability laws. To handle possible variations over time, all descriptors are estimated within a sliding temporal window $(t - w_t, t)$ and readjusted at each iteration. A length w_t fixed at 5 frames ensures a balance between the precision of parameter estimation (that is, D_{local}) and sensitivity to its temporal variation (that is, transient confinement). MTT assigns default typical statistical values to initiate reconnection (from frame 1 to w_t) until past information is available. This does not strongly affect the accuracy of the results as trajectories are long enough (230 frames on average) compared to w_t (5 frames). As reconnection requires information about peak positions, it directly benefits from the detection efficiency. Reciprocally, reconnection strengthens detection efficiency by validating potential new trajectories. Indeed, peaks are first detected with a PFA_{peak} of 10^{-6}, which avoids missing particles. Then, for un-reconnected, orphan peaks, another run of detection is performed with a more stringent PFA_{orphan} of 10^{-7} to provide confidence in putative new trajectories as done for the initial frame.

The informative descriptors used for the reconnection test are defined as follows: (i) a local diffusion characterized with minimal assumption on the mode of diffusion and without excluding possible abrupt variations. The subsequent law adds two probabilities accounting for local and maximum (unconstrained) diffusions, respectively; (ii) an intensity law taking into account blinking (**Supplementary Fig. 1**); and (iii) a disappearance probability for trajectories ended owing to long-lasting blinking or particle leaving the image field, defined by an exponential decay τ_{off}, with a threshold set at $3\tau_{off}$ to stop reconnection. Considering each physical phenomenon as independent, the global likelihood is the product of the probabilities associated with each phenomenon (**Supplementary Note**).

Evaluation of MTT sensitivity and reliability

We validated the MTT input parameters using simulated data to benchmark the performance of MTT at each step (detection, estimation, reconnection). As fluorescence signals are spread over a large range of intensities, a decibel scale was more appropriate. The

fraction of detected peaks was close to 100% (probability of peak detection, $PD_{peak} \approx 1$) for SNR higher than ~20 dB (**Fig. 4a**). This threshold was consistent with the typical experimental values of 20–35 dB (**Supplementary Fig. 1**). Detection was also weakly sensitive to the peak density (**Fig. 4a**). The deflation increased the detection efficiency, substantially approaching the theoretical diffraction limit (**Supplementary Note**) even for densities as high as 10% (10 peaks per 10 × 10 pixels). The error on location (~0.04 pixel = 6 nm) was optimal for all detected particles (down to ~20 dB), reaching the theoretical detection limit (**Fig. 4b** and **Supplementary Note**). For comparison, a three-point estimator[16] appeared inadequate, because its location accuracy was already degraded at 30 dB. Signal integration by the CCD pixels, not included in the model, had almost no effect on location precision (data not shown)[17]. We estimated the tracing accuracy for increasing peak density. Deflation substantially improved the accuracy, which was robust with regard to the underlying diffusion model (**Fig. 4c**). Notably, by reducing the number of critical issues and better handling the remaining ones, MTT is less likely to create artifactual reconnections to nearest neighbors. Use of past statistics is also helpful to adequately resolve crossing particle trajectories (**Supplementary Fig. 2**).

Detection of confinement

Membrane dynamics are expected to involve an interchange of Brownian diffusion and confinement in subdomains[1,4]. We therefore detected confined events on each trajectory according to the equations presented in references 18–22. We computed confinement level L_{conf} as:

$$L_{conf} = D_{max} \times w_{conf}/\mathrm{var}(r), \quad (3)$$

where D_{max} is the unconstrained diffusion coefficient (0.2 μm²/s for EGFR) and var(r) is the variance of the displacements within a

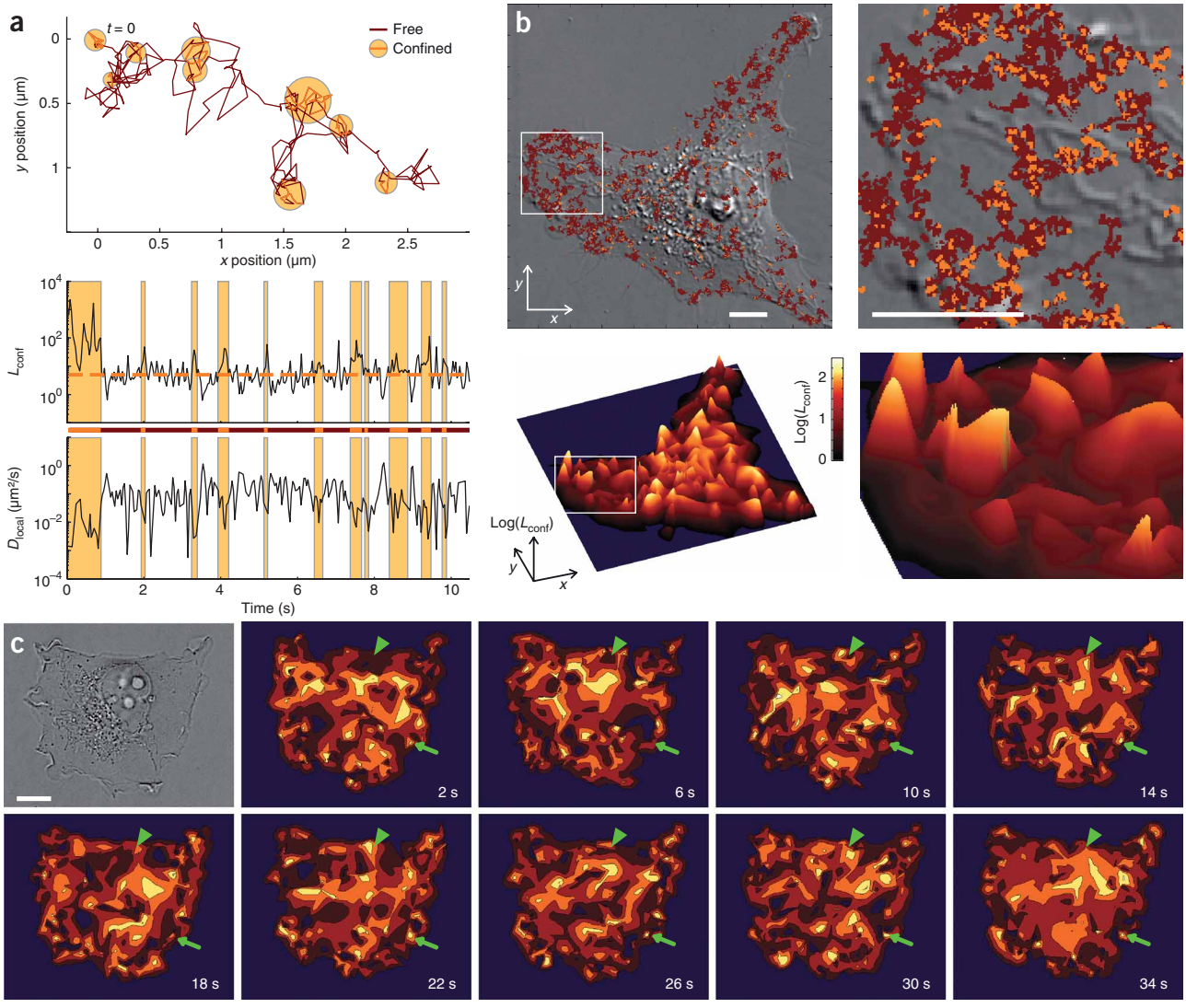

Figure 5 | Detection and mapping of confinement at the cell membrane. (**a**) Typical EGFR trajectory alternating between free and confined events, with corresponding confinement level L_{conf} (middle; threshold depicted by the orange dotted line) and local diffusion D_{local} (bottom). (**b**) Cell map with trajectories (n = 1,200) encoded in two colors as in **a** (left) and a close-up of the boxed area (right). A 3D view of the spatial variations of L_{conf} of the trajectories is shown below. Each step, free or confined, was replaced by its mean (x, y, log(L_{conf})) value, interpolated with Matlab. Color-scale highlights the confinement strength. (**c**) Time-series showing the evolution of the dynamic map, pseudocolored as in **b** (**Supplementary Videos 2** and **3**). Although some confined areas remain stable (arrow), others fluctuate over time (arrowhead). Scale bars, 10 μm.

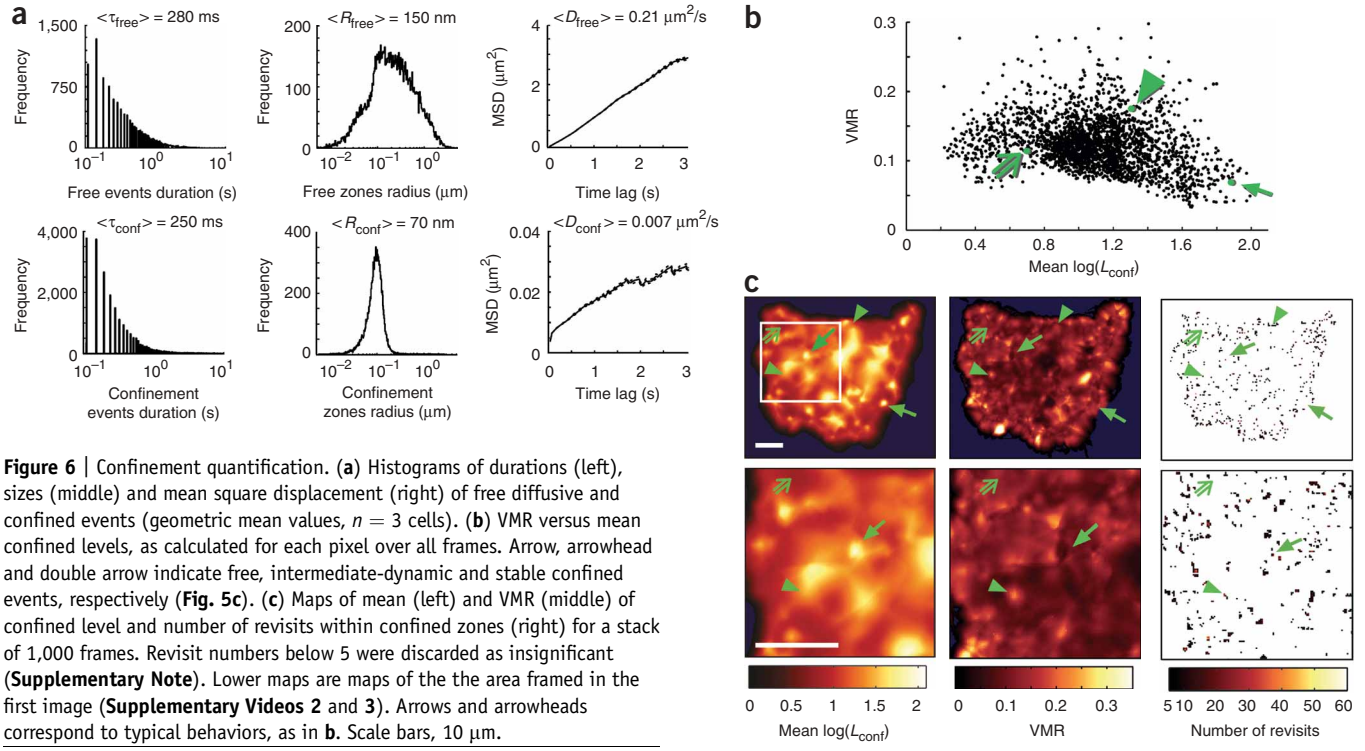

Figure 6 | Confinement quantification. (**a**) Histograms of durations (left), sizes (middle) and mean square displacement (right) of free diffusive and confined events (geometric mean values, $n = 3$ cells). (**b**) VMR versus mean confined levels, as calculated for each pixel over all frames. Arrow, arrowhead and double arrow indicate free, intermediate-dynamic and stable confined events, respectively (**Fig. 5c**). (**c**) Maps of mean (left) and VMR (middle) of confined level and number of revisits within confined zones (right) for a stack of 1,000 frames. Revisit numbers below 5 were discarded as insignificant (**Supplementary Note**). Lower maps are maps of the the area framed in the first image (**Supplementary Videos 2** and **3**). Arrows and arrowheads correspond to typical behaviors, as in **b**. Scale bars, 10 μm.

sliding temporal window of length w_{conf} (**Supplementary Table 1**). A length w_{conf} of 4 frames is both short enough to detect transient confinement and long enough to ensure a reliable detection. Confinement can be statistically assessed when L_{conf} remains over the threshold L_{min} for a sufficient time t_{min} (**Fig. 5a**).

Using simulated data, we aimed to identify threshold values that minimize false detections (low PFA_{conf}) without decreasing the identification of true confinement (high PD_{conf}). A robust method to objectively set the confinement thresholds is to perform a receiver operating characteristics analysis (**Supplementary Fig. 3** online): the values maximizing the global score $PD_{conf} \times (1 - PFA_{conf})$ were 5 for L_{min} and 3 frames for t_{min}. Hence, PD_{conf} can be kept high (0.78) and PFA_{conf} reasonably low (0.025). Notably, as these values came from stable parts of the curves, they have little impact on the overall detection efficiency.

We evaluated confinement detection against various models: transient slowdown, permeable domains, anomalous diffusion or free diffusion (**Supplementary Fig. 4** online). Our confinement detector searched for local disparities instead of global, large-scale variations as for anomalous diffusion. Consistent with this hypothesis, MTT detected slowdowns and domains better than anomalous behavior, which rendered results comparable to free diffusion.

Cartography of EGFR dynamics in live cells

We tested the principle of cartography by generating a snapshot of the membrane dynamics for the EGFR at the surface of live COS-7 cells. We projected up to 1,200 trajectories with ~230 frames on average recorded over a short period of time (10 s, 300 frames/stack) onto the differential interference contrast image of the cell (**Fig. 5b**; pixel size 160 nm). In a static three-dimensional (3D) representation, the peak height equals the strength of confinement, whereas valleys relate to few or no confinement (**Fig. 5b**). For a more dynamic view, we investigated the confinement frame by frame over longer periods of time (**Fig. 5c**, and **Supplementary Videos 2** and **3** online). This temporal analysis simultaneously revealed stable and evanescent confined areas. We also noticed rare linear motion (<2%), as expected for endocytic vesicles[23].

We observed transitions between various regimes of diffusion, characterized by a wide range in duration (0.1–10 s), size (0.01–1 μm) and strength (1–100) (**Fig. 6a** and **Supplementary Fig. 3**). These values corroborate the transient confinement zones observed using a similar confinement detection method[18] for a glycosyl-phosphatidylinositol–anchored protein Thy1 and a glycosphingolipid, GM1. Compared to free-diffusion events, confined periods are characterized by smaller submicrometer sizes (70 ± 1 nm, $n = 5$ cells), although with similar subsecond duration (250 ± 15 ms). The fraction of confined time accesses the fraction α_{conf} of confined receptors (0.40 ± 0.05). Similarly, the fraction of confined area was 0.08 ± 0.02. We next quantified the confinement diversity using statistic descriptors of confinement levels calculated from the values displayed in the movies. A dot plot of variance-to-mean ratio (VMR) versus mean revealed a broad distribution of both descriptors (**Fig. 6b**). Regimes continuously ranged from free diffusion (low mean) to high confinements (high mean), both of which were stable over time (low VMR). However, most events displayed intermediate confinement with high VMR, suggesting dynamic structures. We located these different regimes by mapping the descriptors in color-encoded maps (**Fig. 6c**). The dynamics of confinement structures can also be assessed by determining their stability over time. A straightforward evaluation is to quantify the revisit frequency of confined areas. Counting the number of confined events associated to each pixel revealed highly revisited areas (**Fig. 6c**). Considering variance, frequently revisited areas mostly correlated with intermediate confinement. We probed a

representative population of EGFR (~1%). Thus, a rate of 50 visits within a 36-s recording (1.4 visits/s) would correspond for the whole population to more than 100 visits/s. This confirms sub-second dwell time ranges (<10 ms) for the most dynamic events.

This representation of confinement relies on spatiotemporal characteristics, resulting from the density of targets and the overall exposure time (camera readout). Both parameters must balance experimental limitations and biological relevance. We therefore made measurements at increased acquisition speed (**Supplementary Fig. 5** online). MTT remained efficient down to 5 ms/frame, with an acceptable SNR (~25 dB), allowing valuable investigations.

DISCUSSION

Single EGFR tracking has previously been performed to study signal transduction[10,24] and membrane dynamics[25]. The EGFR cartography built using MTT provides a global view of molecular dynamics. Notably, the statistics built from individual observations are in excellent agreement with SPT[25]. This demonstrates that, on top of providing a snapshot of the spatiotemporal dynamics of large cell membrane areas, each trajectory is accurately reconnected by MTT. Confinement owing to submembrane cytoskeletal fences[6,26], lipid domains[6,27] and direct[19] or long-range[28] protein interactions is a major factor of membrane organization[1,4]. Our measurements reveal a partial confinement into sub-micrometer domains, consistent with transient confinement zones[18], reminiscent of a preferential partition in lipid-dependent domains[29,30]. Notably, the confinement profile presents a broad distribution of strength (**Supplementary Fig. 3**). This may reflect an underlying diversity and complexity of confining processes. Nevertheless, this apparent diversity may also arise from a large spread of affinities, leading to a large distribution of escape times[21]. Owing to our higher spatiotemporal resolution, the observations for EGFR on confinement sizes, dwell times and mean square displacement refine previous SPT observations[25]. We found transient confinement (~250 ms) into small domains (<100 nm) (**Fig. 6**), which are consistent with local measurements obtained by FCS (F. Conchonaud & D.M., unpublished data). For confined events, the mean square displacement consistently displays a negative deviation[1]. The decrease in diffusion directly relates to the local viscosity. The biochemical nature of the underlying heterogeneities could derive from coexisting lipid-dependent and actin-mediated domains. EGFR transient confinement was as efficiently modeled by alternating fast and slow diffusion as by permeable domains, in agreement with either dynamic partition or corralling. Possible anomalous diffusion could be investigated by a generalized approach to detect putative obstacles at various length scales. This would further minimize our initial assumptions for the confinement detection as described for the detection, evaluation and reconnection steps.

This project is ultimately aimed at elucidating how the dynamic organization of the plasma membrane influences cellular responses. This requires improving performance related to the two major SPT limitations[7]: the acquisition speed (relates to SNR), and single-fluorophore discrimination (particle density) (**Fig. 4**). Fast SPT acquisition is critical for inherently fast movements like lipid diffusion[27], rapid transient confinement[26] and 3D motion such as virus trafficking[31]. MTT has proven to be sensitive at fairly low SNR, allowing working with reduced light intensity (limited photodamage), less bright dyes, or increased acquisition speed (**Supplementary Fig. 5**). Evaluating tracking performances is linked to the biological question. For instance, a minimal length of errorless trajectories is required to discriminate anomalous diffusion from confinement. The ultimate limitation will occur at the transition between individual labeling and uniform staining corresponding to a density of ~10%, when fluorescent peaks start to strongly overlap (**Supplementary Note**). This theoretical limit can be tackled considering new photoactivation-based techniques (photoactivation localization microscopy (PALM), fluorescence PALM (FPALM) and stochastic optical reconstruction microscopy (STORM))[32] offering a promising alternative for exhaustive and resolved imaging. With sptPALM[33], substantial improvement in the rate of imaging (20 frames/s) allowed tracking of photo-activated molecules appearing during the course of hundreds of seconds. A diffusion map of membrane proteins has similarly been established based on the longest trajectories (>15 frames), which represent 3% of all molecules[33]. Using a more conventional setup, MTT provides a robust and complementary analytical tool for refined diffusion analysis. Additional developments, including multicolor imaging, will expand MTT to a new spectral dimension. Simultaneous *in situ* measurements of different signal transduction partners will enable investigation into spatiotemporal distributions and kinetic interactions. This new and sensitive approach will provide a detailed view of membrane dynamics, linking local characteristics and heterogeneities with physiological implications.

METHODS

Software. We analyzed the data by custom algorithms written with Octave (GNU) and Matlab (MathWorks). A detailed description of the MTT algorithm is available in the **Supplementary Note**. The source code of the MTT software is available online (http://www.ciml.univ-mrs.fr/lab/he-marguet.htm); academic and nonprofit use is free of charge.

Additional methods. Methods for Monte Carlo simulations, cell culture, Qdot staining, and equipment and settings are available in **Supplementary Methods** online.

Note: Supplementary information is available on the Nature Methods website.

ACKNOWLEDGMENTS

We thank H.T. He, L. Leserman, P. Réfrégier, F. Conchonaud, S. Mailfert and M. Fallet for helpful discussions and suggestions, and E. Witty (AngloScribe) for language editing. This project was supported by grants from Institut National de la Santé et de la Recherche Médicale, Centre National de la Recherche Scientifique, Agence Nationale de la Recherche and European regional development fund.

AUTHOR CONTRIBUTIONS

H.R. and D.M. designed the research; A.S. and N.B. performed the research, developed new analytical tools and analyzed data; A.S. and D.M. wrote the paper.

Published online at http://www.nature.com/naturemethods/
Reprints and permissions information is available online at http://npg.nature.com/reprintsandpermissions/

1. Saxton, M.J. & Jacobson, K. Single-particle tracking: applications to membrane dynamics. *Annu. Rev. Biophys. Biomol. Struct.* **26**, 373–399 (1997).
2. Lippincott-Schwartz, J., Altan-Bonnet, N. & Patterson, G.H. Photobleaching and photoactivation: following protein dynamics in living cells. *Nat. Cell Biol.* **5** (Suppl.), S7–S14 (2003).
3. Lommerse, P.H., Spaink, H.P. & Schmidt, T. In vivo plasma membrane organization: results of biophysical approaches. *Biochim. Biophys. Acta* **1664**, 119–131 (2004).

4. Marguet, D., Lenne, P.F., Rigneault, H. & He, H.T. Dynamics in the plasma membrane: how to combine fluidity and order. *EMBO J.* **25**, 3446–3457 (2006).
5. Wawrezinieck, L., Rigneault, H., Marguet, D. & Lenne, P.F. Fluorescence correlation spectroscopy diffusion laws to probe the submicron cell membrane organization. *Biophys. J.* **89**, 4029–4042 (2005).
6. Lenne, P.F. *et al.* Dynamic molecular confinement in the plasma membrane by microdomains and the cytoskeleton meshwork. *EMBO J.* **25**, 3245–3256 (2006).
7. Meijering, E., Smal, I. & Danuser, G. Tracking in molecular bioimaging. *IEEE Signal Process. Mag.* **23**, 46–53 (2006).
8. Michalet, X. *et al.* Quantum dots for live cells, *in vivo* imaging, and diagnostics. *Science* **307**, 538–544 (2005).
9. Dahan, M. *et al.* Diffusion dynamics of glycine receptors revealed by single-quantum dot tracking. *Science* **302**, 442–445 (2003).
10. Lidke, D.S. *et al.* Quantum dot ligands provide new insights into erbB/HER receptor-mediated signal transduction. *Nat. Biotechnol.* **22**, 198–203 (2004).
11. Schmidt, T., Schutz, G.J., Baumgartner, W., Gruber, H.J. & Schindler, H. Imaging of single molecule diffusion. *Proc. Natl. Acad. Sci. USA* **93**, 2926–2929 (1996).
12. Kalaidzidis, Y. Intracellular objects tracking. *Eur. J. Cell Biol.* **86**, 569–578 (2007).
13. Schlessinger, J. Ligand-induced, receptor-mediated dimerization and activation of EGF receptor. *Cell* **110**, 669–672 (2002).
14. Tang, J. & Marcus, R.A. Mechanisms of fluorescence blinking in semiconductor nanocrystal quantum dots. *J. Chem. Phys.* **123**, 054704 (2005).
15. Cheezum, M.K., Walker, W.F. & Guilford, W.H. Quantitative comparison of algorithms for tracking single fluorescent particles. *Biophys. J.* **81**, 2378–2388 (2001).
16. Bonneau, S., Dahan, M. & Cohen, L.D. Single quantum dot tracking based on perceptual grouping using minimal paths in a spatiotemporal volume. *IEEE Trans. Image Process.* **14**, 1384–1395 (2005).
17. Ober, R.J., Ram, S. & Ward, E.S. Localization accuracy in single-molecule microscopy. *Biophys. J.* **86**, 1185–1200 (2004).
18. Dietrich, C., Yang, B., Fujiwara, T., Kusumi, A. & Jacobson, K. Relationship of lipid rafts to transient confinement zones detected by single particle tracking. *Biophys. J.* **82**, 274–284 (2002).
19. Meier, J., Vannier, C., Serge, A., Triller, A. & Choquet, D. Fast and reversible trapping of surface glycine receptors by gephyrin. *Nat. Neurosci.* **4**, 253–260 (2001).
20. Meilhac, N., Le Guyader, L., Salome, L. & Destainville, N. Detection of confinement and jumps in single-molecule membrane trajectories. *Phys. Rev. E* **73**, 011915 (2006).
21. Saxton, M.J. Single-particle tracking: effects of corrals. *Biophys. J.* **69**, 389–398 (1995).
22. Simson, R., Sheets, E.D. & Jacobson, K. Detection of temporary lateral confinement of membrane proteins using single-particle tracking analysis. *Biophys. J.* **69**, 989–993 (1995).
23. Wiley, H.S. Trafficking of the ErbB receptors and its influence on signaling. *Exp. Cell Res.* **284**, 78–88 (2003).
24. Teramura, Y. *et al.* Single-molecule analysis of epidermal growth factor binding on the surface of living cells. *EMBO J.* **25**, 4215–4222 (2006).
25. Orr, G. *et al.* Cholesterol dictates the freedom of EGF receptors and HER2 in the plane of the membrane. *Biophys. J.* **89**, 1362–1373 (2005).
26. Kusumi, A. *et al.* Paradigm shift of the plasma membrane concept from the two-dimensional continuum fluid to the partitioned fluid: high-speed single-molecule tracking of membrane molecules. *Annu. Rev. Biophys. Biomol. Struct.* **34**, 351–378 (2005).
27. Schutz, G.J., Kada, G., Pastushenko, V.P. & Schindler, H. Properties of lipid microdomains in a muscle cell membrane visualized by single molecule microscopy. *EMBO J.* **19**, 892–901 (2000).
28. Daumas, F. *et al.* Confined diffusion without fences of a g-protein-coupled receptor as revealed by single particle tracking. *Biophys. J.* **84**, 356–366 (2003).
29. Puri, C. *et al.* Relationships between EGFR signaling-competent and endocytosis-competent membrane microdomains. *Mol. Biol. Cell* **16**, 2704–2718 (2005).
30. Yamabhai, M. & Anderson, R.G. Second cysteine-rich region of epidermal growth factor receptor contains targeting information for caveolae/rafts. *J. Biol. Chem.* **277**, 24843–24846 (2002).
31. Seisenberger, G. *et al.* Real-time single-molecule imaging of the infection pathway of an adeno-associated virus. *Science* **294**, 1929–1932 (2001).
32. Moerner, W.E. Single-molecule mountains yield nanoscale cell images. *Nat. Methods* **3**, 781–782 (2006).
33. Manley, S. *et al.* High-density mapping of single-molecule trajectories with photoactivated localization microscopy. *Nat. Methods* **5**, 155–157 (2008).